ARTICLE

Modulating Surface Redox Reactions and Solvated Electron Emission on Boron-Doped Diamond by (Photo)Electrochemistry

Arsène Chemin[1], Louis Godeffroy[1], Marin Rusu[1], Michael Drisch[2], Maik Finze[2], Peter Knittel[3], Anke Krueger[2,4], Tristan Petit[1]

[1] Helmholtz-Zentrum Berlin für Materialien und Energie GmbH, Hahn-Meitner-Platz 1, 14109
[2] Institute for Organic Chemistry, Julius-Maximilians University Würzburg, Am Hubland, 97074, Würzburg, Germany
[3] Fraunhofer-Institut für Angewandte Festkörperphysik Freiburg DE
[4] Institute for Organic Chemistry, Stuttgart University, Pfaffenwaldring 55, 70569 Stuttgart, Germany

Abstract

The interplay between photo- and electrochemical reactions fundamentally influences charge transfer processes at solid-liquid interfaces. Nevertheless, chemical processes at semiconductor surfaces triggered by light excitation under applied potential remain poorly explored. This work deciphers the synergistic role of potential and light excitation on boron-doped diamond electrodes in producing either surface redox reactions or emission of solvated electrons in water. The role of diamond surface termination on electron affinity, band bending, and charge extraction is identified in a photoelectrochemical cell. While photocurrent is observed for excitation as low as 3.5 eV, we show that it is mostly induced by surface redox reactions, whereas solvated electrons are detected only for excitation above the bandgap (5.47 eV). Solvated electrons are generated irrespective of band bending, which only affects the emission yield. Depending on the surface band bending, photoreduction of the hydroxylated surface groups and photooxidation of the -H surface groups can be induced by direct photoexcitation in the range of 4.2-4.8 eV. The surface of the diamond can be electrochemically reduced when the Fermi level of the oxidized surface decreases below the H^+/H_2 redox potential. On the other hand, the hydrogenated surface oxidizes spontaneously for potentials at which the Fermi level drops below the occupied CH surface states, depending on both the pH and electron affinity of the surface. This work provides fundamentally new insights into (photo)redox processes on diamond materials, which may find applications in photoelectrochemical solar fuel generation or energy storage.

2. Broader context

Photoelectrochemistry using renewable solar energy will play an essential role in the energy transition to a decarbonized society. There is an urgent need to develop sustainable electrodes with excellent stability, photoactivity, and selectivity. Due to rapidly decreasing fabrication costs and scalable synthesis, synthetic boron-doped diamond is attracting interest for this purpose. It constitutes an ideal metal-free electrode material for electrochemical reactions under harsh conditions, such as water decontamination, due to its wide potential window, exceptional stability, and robustness. Diamond also serves as a source of solvated electrons when excited by UV light, allowing the chemical reduction of CO_2 and N_2 molecules. Understanding the complex interactions at the interface between diamond and the electrolyte upon photoexcitation and potential variation is crucial for designing competitive diamond materials with excellent performance for future photochemical applications.

3. Introduction

As an alternative to fossil fuels, chemical products derived from renewable and abundant solar energy, also known as “solar fuels”, are attracting increasing attention. The simplest way to produce solar fuels such as H_2, C_2H_2 or CH_3OH among others is by coupling standard photovoltaic cells to electrolysers. Taking advantage of the maturity of these two technologies, this approach enabled a fast development of solar fuels which are now close to reaching the market. However, to prevent additional efficiency losses due to external coupling, direct photoelectrochemical (PEC) conversion would be preferable.[1] PEC uses wide bandgap (>1.5 eV) semiconducting materials (e.g. TiO_2, Cu_2O, Fe_2O_3, etc.) as light absorbers.[2] For large enough bandgaps, the photon energy can compensate for the overpotential needed for the electrochemical reaction and the reduced working potential helps saving electrical power as well

as increasing selectivity. PEC experienced a significant revival following the use of high surface area nanostructured electrodes inspired by the design of dye-sensitized colloidal TiO_2 films by O'Regan and Grätzel.[3] Since then, a variety of materials and strategies have been explored to enhance the effectiveness of PEC, yet numerous challenges persist.

TiO_2 remains the most used semiconductor in photocatalysis because of its low cost, chemical stability, and high oxidizing power. However, the recombination of electron-hole pairs hinders its activity under visible irradiation.[4] Cu_2O, otherwise more effective, degrades very quickly due to surface states poisoning and recent studies have focused on understanding and mitigating this rapid degradation.[5] Hematite (α-Fe_2O_3) has also been extensively studied as a photoanode material due to its record-high theoretical photocurrent for water oxidation (based on its relatively narrow bandgap of 1.9-2.2 eV) and chemical stability.[6] But recent studies have demonstrated that only a small fraction of the theoretical photocurrent could ever be reached for hematite photoanodes.[7]

Optimizing photoactive materials often involves focusing separately on stability, light absorption, charge transfer, and photoelectroactivity. However, bulk electronic properties and *ex situ* characterizations do not fully explain behaviors under operating conditions. PEC requires stable materials and a good understanding of the interface properties[8] and photoexcitation processes in order to limit charge trapping and electron-hole recombination pathways.[9] Catalytic reactions are highly sensitive to surface chemistry and the surface termination can significantly modify the band structure of semiconductors, changing the electron affinity and surface band bending. The interplay between these interface properties along with applied potential and equilibrium with the electrolyte, significantly influences the overall behavior of the electrode.[9,10] Therefore, a comprehensive analysis that combines interface characterization, photoexcitation, and charge transfer in relation to applied potential is necessary to grasp the fundamental electrode properties and improve its performances.

Due to recent improvements in their production, synthetic boron-doped diamonds (BDD) are attracting interest with rapidly decreasing fabrication costs and scalable synthesis.[11] BDD is an ideal material for metal-free electrodes for electrochemical reactions under harsh conditions, such as water decontamination, due to its excellent chemical stability, conductivity and sustainability.[12–14] In the context of direct solar-to-fuel conversion, diamond stands out as a unique photoelectrode material emitting solvated electrons under UV light when doped with boron,[15] and visible light for detonation nanodiamonds,[16] unlocking challenging reactions such as nitrogen[17] and carbon dioxide reduction[18–21]. However, photoelectron yields remain limited and the coupling of photo- and electrochemical processes at the diamond-water interface remain poorly understood. Unraveling the mechanisms at play is crucial for finding new strategies to improve solvated electron emission, diamond photoactivity, and selectivity.

Diamond has the specificity of accommodating a broad range of surface terminations (such as H, O, N, F), which may introduce new electronic states within the bandgap.[22,23] We have recently demonstrated in air that these surface states can be excited in the visible range, despite the inherently wide bandgap of diamond.[24] We suggest that this mechanism may be responsible for the photocurrent observed in the literature,[25–29] whose origin is still debated. Although this photocurrent has a low yield, it is applicable in specialized fields such as brain implants[29–32] and photoelectrochemistry.[33,34] Distinguishing photocurrent induced by redox reactions involving surface states from the emission of solvated electrons is crucial for assessing the chemical reactivity of diamond in aqueous electrolytes.

In this study, we combine photoelectrochemical and spectroscopic methods to comprehensively analyze the BDD|water interface of nanostructured BDD under illumination and applied potential, in conditions relevant to producing solar fuels. The characterization of electron affinity, band bending, and charge extraction during photoelectrochemical processes on BDD enhances our understanding of semiconductor|water interfaces. Dosing of solvated electrons enables the differentiation between light excitation leading to redox reactions at the surface of the diamonds and the emission of solvated electrons. Photocurrent-Cyclic Voltammetry is introduced to provide evidence of electrochemical oxidation and reduction of the surface and spontaneous oxidation in water. This comprehensive insight into the photo/electrochemical reactivity of BDD interfaces will allow the design of more efficient diamond-based photoelectrodes in the future. The methodologies introduced will also have the potential to improving other photoelectrode materials.

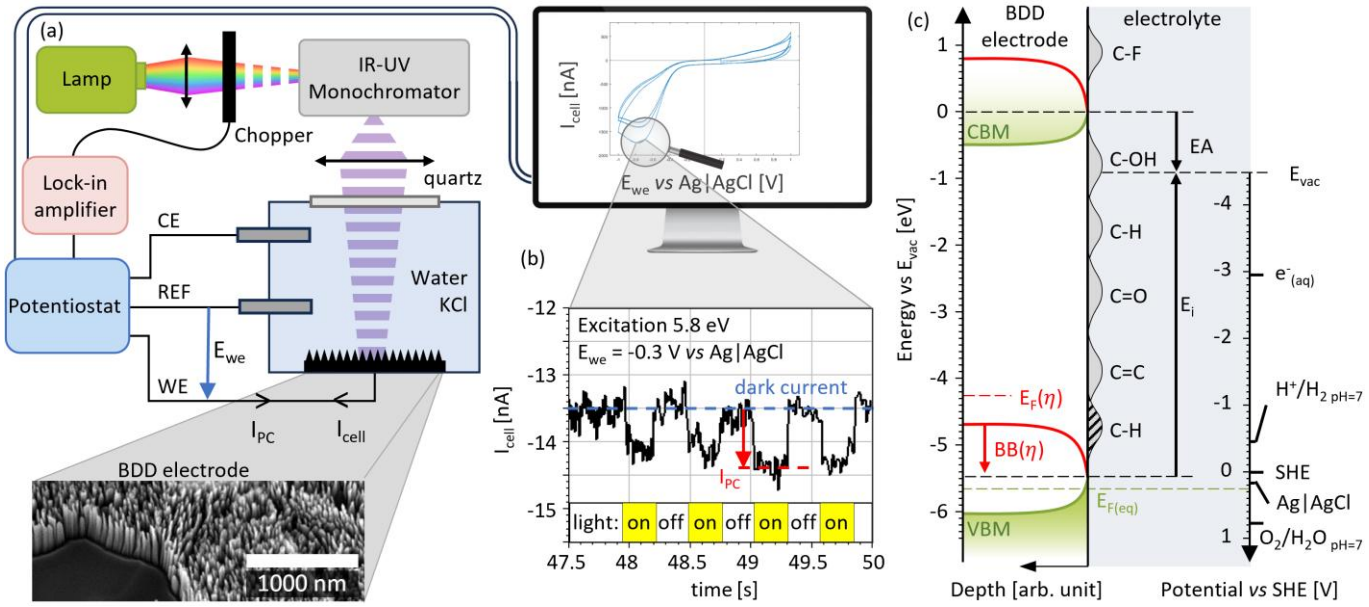

Figure 1: Photocurrent spectroscopy on nanostructured BDD electrodes. (a) Scheme of the photoelectrochemical cell and sign conventions, and cross-sectional SEM view of the nanostructured BDD electrodes used in this study. (b) Cell current I_{cell} measured by the potentiostat and photocurrent I_{PC} due to the illumination of the electrode. (c) Band diagram of electrode and surface states in equilibrium with water and definition of the electron affinity $EA = E_{vac} - E_{CBM}$, ionization energy $E_i = E_{vac} - E_{VBM}$, and band bending $BB(\eta) = E_F(FBP) - E_F(\eta)$ for a given flat band potential (FBP) and applied potential (η). The positions of the surface states are deduced from X-ray absorption spectroscopy as detailed in SI (fig. S1).

4. Results and discussion

4.1. Photocurrent Spectroscopy

Nanostructured polycrystalline BDD with needle-like structures of about 100 nm, as shown in the cross-section SEM image presented in fig. 1a, were used in this study[18]. These electrodes have similar bulk properties to polycrystalline BDD while exhibiting increased charge transfer reactions at the interface due to nanostructuring[18,35–37].

The BDD electrodes are studied as the working electrode (WE) in a three-electrode photoelectrochemical cell presented in fig. 1a. The measurements have been carried out in 3 M KCl electrolyte ensuring a good ionic conductivity and limiting the influence of the diffusion processes in the Helmholtz layer. While the potential and current are controlled by a potentiostat, the modulated illumination (1.8 Hz) of the WE at a chosen energy is set by a monochromator. The photocurrent is extracted either directly from the cell current recorded by the potentiostat, as presented in fig. 1b, or using a lock-in detection enabling great sensitivity to small photocurrents down to pA. The photocurrent is not capacitive, and no spikes are observed. Contrary to the cell current, the photocurrent is considered positive when it flows from the counter electrode (CE) to the WE, accounting for the solvated electrons current as positive. Since the photocurrent is much smaller than the overall cell current, the effect of light excitation on the band bending and polarization of the electrode will be considered negligible in the following discussion.

The band alignment at the diamond|water interface is presented in fig. 1c. At the surface, the energy difference between the conduction band minimum (CBM) and the vacuum energy level is defined as the electron affinity (EA) and strongly depends on the surface termination.[24,38,39] The position of the valence band maximum (VBM) at the surface is 5.47 eV below, corresponding to the bandgap of diamond. In the bulk, the Fermi level (E_F) at equilibrium is pinned to the level of the doping states, in our case about 0.39 eV above the VBM.[40] The equilibrium of this Fermi level with the chemical potential of the electrolyte (green dashed line) leads to a surface charge transfer, the formation of a space charge region at the surface of the diamond and an associated surface band bending (green solid lines). This charge transfer is in fact responsible of the surface conductivity of hydrogenated diamonds in water as the VBM is above the Fermi level at the surface.[41–44]

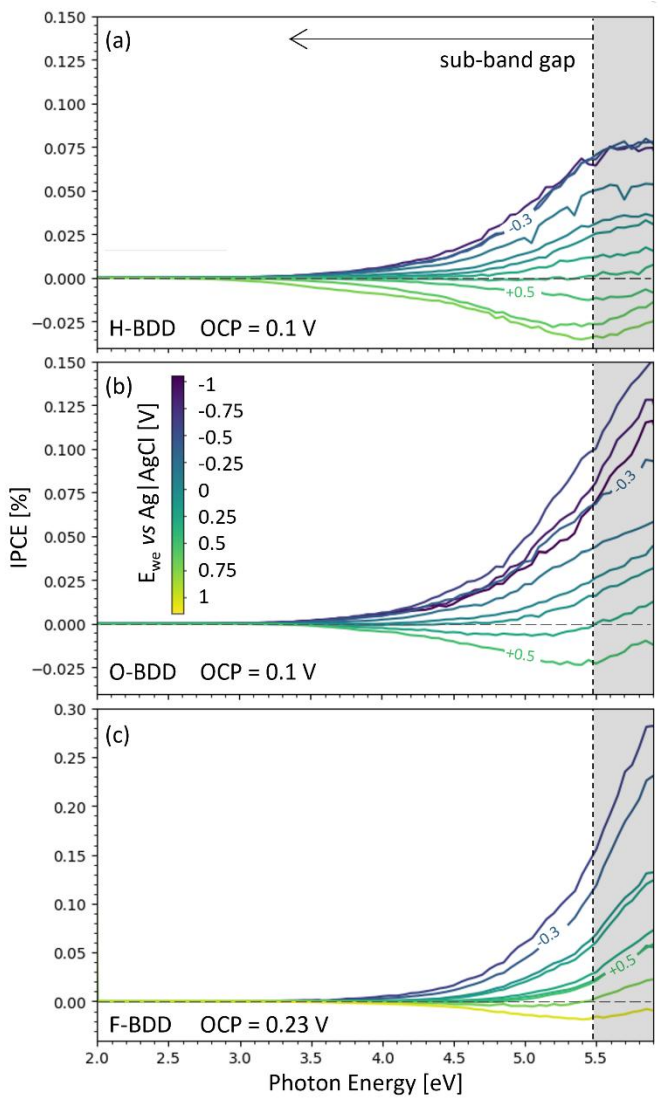

Figure 2: Role of diamond surface termination on photocurrent. IPCE recorded on H-BDD (a), O-BDD (b), and F-BDD (c) in 3M KCl electrolyte for different applied potential versus Ag|AgCl reference electrode. The color scale is the same in all three plots for easier comparison, but the potential ranges applied to the different samples have been adjusted to account for their different band bending and open circuit potential (OCP) characteristics which depend on surface chemistry. The vertical dashed lines correspond to the bandgap energy.

When a potential E_{we} is applied, the Fermi level shifts accordingly in the bulk BDD electrode by a value η (red dashed line) and thus modifies the surface band bending (red solid lines). η cannot be directly measured as E_{we} because of ohmic drops and contact potentials in the real PEC cell. Yet, only a negligible fraction of any applied potential appears across the Helmholtz layer,[45] and the remaining difference can be measured as explained in the SI section 8.

The EA of the surface can be determined by measuring the ionization energy (E_i) by photoelectron yield spectroscopy (PYS), as presented in fig. S6 and table S1. Contrary to UV photoelectron spectroscopy (UPS) and X-ray emission spectroscopy (XES), which are performed under vacuum, PYS is conducted at atmospheric pressure with adsorbed water molecules. The contact with these adsorbed molecules is sufficient to induce charge transfers similar to those observed between the electrode and the redox couples (involving oxygen and water) in the electrolyte.[41] The values of ionization energy and EA measured in this manner are assumed to remain valid in the electrolyte and further discussed later. In contrast to most semiconductors, diamond electrodes have molecular surface states due to their termination. These states can exist within the bandgap, where electrons can be excited upon light excitation, and, similar to surface defects, they can lead to charge trapping.[24,46,47] The position of these surface states can be determined by X-ray absorption spectroscopy (XAS), as presented in fig. S1 and summarized in fig. 1c. The associated charge transfers due to direct photoexcitation or charge trapping have been identified in air by surface photovoltage measurements[24], but their role in the photoelectrochemical properties of diamond electrodes has not yet been precisely identified. Both oxygen and hydrogen-terminated surfaces present surface states within the diamond bandgap, while fluorinated surfaces do not.[48,49] In the following, we use these properties to identify the photocurrent due to surface states by comparing these three surface terminations.

The incident photon-to-current efficiency (IPCE) measured on the BDD with H-, O- and F-terminations as a function of the applied potential and excitation photon energy is shown in fig. 2. While the H-termination was achieved by a plasma, O and F where obtained wet-chemically. For all surface chemistries, stronger photocurrent is observed above the bandgap (5.47 eV) due to direct band-to-band excitation. However, a significant photocurrent is also observed below the bandgap for O-BDD and H-BDD, starting from about 3.5 eV, as previously observed[24]. In contrast, F-BDD shows a much-reduced sub-bandgap photocurrent, regardless of the applied potential. Sub-bandgap photocurrent is indeed strongly related to the presence of hydroxylated and hydrogenated surface states within the diamond bandgap, as illustrated in fig. 1**c**. The photoexcitation of sp^2 surface states has often been considered as a possible origin of photocurrent.[31,50] Yet, F-BDD shows more sp^2 than O-BDD and H-BDD (see SI fig. S1), challenging this hypothesis. Furthermore, sp^2 surface states are excited at 0.7 eV and around 1.5 eV[24] while no photocurrent is measured below 3.5 eV. Similarly, the excitation of $\pi^*_{C=O}$ surface states, between 2.25 and 3.3 eV,[24] can be discarded.

For applied potentials between -0.3 and +0.5 V *vs* Ag|AgCl, the photocurrent observed on H-BDD and O-BDD is nearly identical, despite starting the measurements at the open circuit potential (OCP) to limit electrochemical modification of the surface. It suggests the spontaneous oxidation of the H-BDD surface upon contact with water as previously identified using near ambient pressure X-ray photoelectron spectroscopy (NAP-XPS).[18] The reason of this spontaneous oxidation will be discussed later.

4.2. Photo-redox Reactions and Emission of Solvated Electrons

To determine the origin of the photocurrent, we quantified the amount of solvated electrons emitted by O-BDD over 1h of constant light exposure, as a function of applied potentials, by fluorimetry (see SI fig. S7 for details).[51] Briefly, a small amount of NO_3^- is added to the electrolyte, which plays the role of electron scavenger to form NO_2^-. After the experiment, the electrolyte is recovered and reacted with 2,3-diaminonaphthalene, which in the presence of NO_2^- undergoes a diazotation reaction to form the very sensitive fluorescent probe 1-[H]-naphthotriazole. The NO_2^-concentration allows then the quantification of the solvated electron concentration as shown in fig. 3b. A control experiment is performed in the dark at -0.5 V (left dashed bar) to demonstrate that no $NO_2^-$is generated electrochemically as the amount detected by fluorescence corresponds to the detection limit (see fig. S7). At 0.1 V, for excitation at 4.5 eV, below the bandgap (central dashed bar), no solvated electrons were detected, as there is no detectable difference compared to the control experiment. Hence, the photocurrent measured below the bandgap is only due to the excitation and redox reaction of the surface groups. For excitation above the bandgap energy, the amount of solvated electrons increases for more negative potentials and depends strongly on the surface band bending.

The surface band bending can be estimated as the difference between the applied potential and the flat band potential (FBP). A usual way to determine the FBP of classical semiconductor electrodes, known as the Gärtner–Butler analysis, is to plot the photocurrent intensity generated by excitation above the bandgap with respect to the applied potential as represented in fig. 3a.[52] The dark grey dashed lines correspond to a *Schottky barrier* model fitted on the data. A *Schottky* behavior is expected when the current is not limited by chemical processes or by ion diffusion in solution, but only by the rate at which the excited carriers approach the surface.[2,45] These assumptions are valid here because the emission of solvated electrons from the diamond surface is not mediated by any chemical reaction and the ion concentration in solution is large. The photocurrent is thus determined as:

$$I_{PC} = I_{PC}^{0}[exp(-\eta q/nkT) - 1] \qquad (1)$$

with I_{PC}^{0} the saturation current, $\eta \simeq E_{WE} - FBP$ the applied potential expressed with respect to the FBP, q the elementary charge, k the Boltzmann constant, T the temperature and n the ideality factor that accounts for the recombination of charge carriers. Simply, at the FBP, the photocurrent is close to zero because there is no driving force to separate the photogenerated charge carriers. When a negative potential is applied, the electric field in the space-charge region increases, enhancing the separation of electron-hole pairs and driving the electrons in the conduction band towards the surface of the diamond.

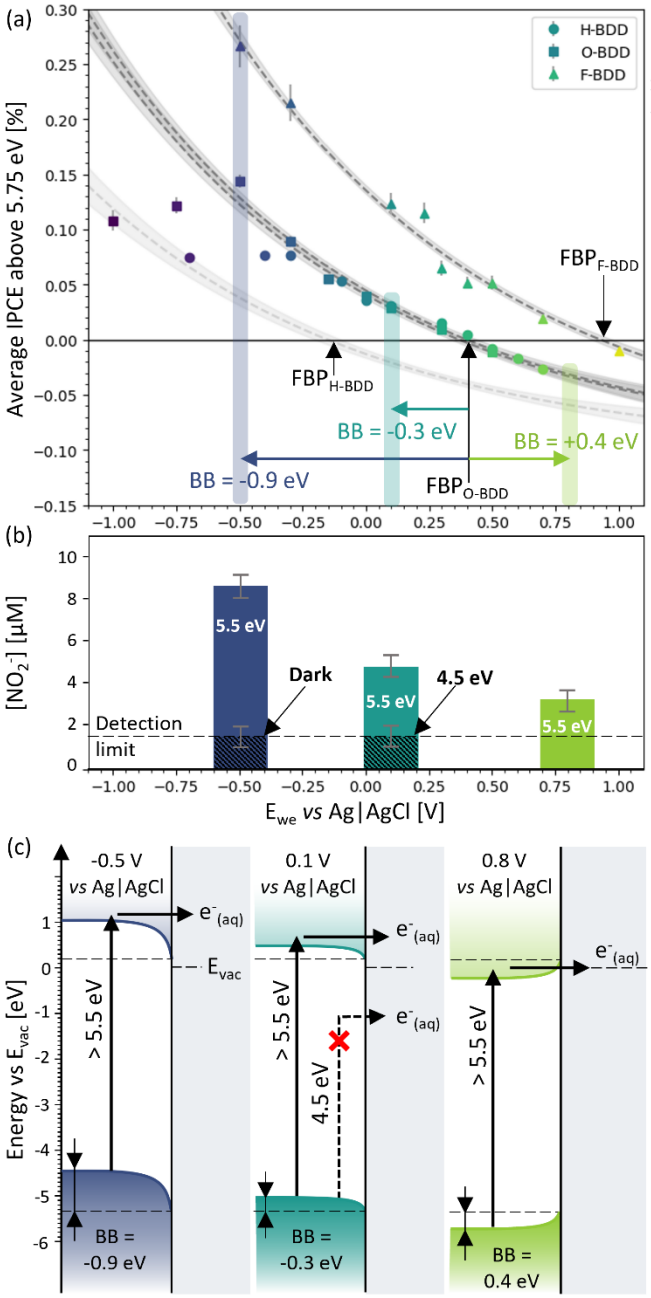

The *Schottky barrier* model is fitted on the O-, H- and F-BDD data, changing only the FBP which is dependent on the surface

Figure 3: Photoexcitation of diamond electrodes above the bandgap. (a) Average IPCE for excitation above 5.75 eV at different potentials for H-BDD (circles), O-BDD (squares), and F-BDD (triangles). The dashed lines correspond to fits considering *Schottky barrier* models for different flat band potential (FBP) (black arrows). Colored arrows show the band bending observed under the conditions used for dosing the solvated electrons. (b) NO_2^-concentration measured by fluorimetry, which relates to the amount of emitted solvated electrons. (c) Schemes of the origin of the solvated electrons depending on the band bending and the excitation energy. The EA (determined by PYS measurement in fig. S6) and FBP correspond to the O-BDD sample.

states. The IPCE corresponding to the saturation current is 0.10 ± 0.02 %. The ideality factor, $n = 43 \pm 5$, is very large, showing a significant recombination of charge carriers, strongly hindering the emission yield. The FBP of H-BDD and O-BDD are respectively 0.37 ± 0.03 V and 0.40 ± 0.04 V. It is again evident that both surfaces are very similar due to the spontaneous surface oxidation of H-BDD in water. The FBP of the F-BDD is much larger, 0.93 ± 0.04 V, because the EA of the fluorinated surface is larger, as measured by PYS in the SI fig. S6.

For potentials below -0.3 V *vs* Ag|AgCl, one can observe that the measurements diverge from the theoretical curves (dashed lines in fig. 3a) in the case of the O- and H-BDD. At these negative potentials, the surface undergoes electrochemical reduction, as discussed in more detail later, and these points were not considered for the fit. As a consequence, the EA and FBP are reduced, leading to a shift in the theoretical curve to the left until it reaches that of a fully hydrogenated surface (dashed light grey curve in fig. 3a) with an FBP of about -0.15 V. The three colored arrows correspond to the band bending at the potentials applied on O-BDD for which the solvated electrons were quantified. As illustrated in fig. 3**c**, downward band bending of -0.9 V and -0.3 V is observed at -0.5 V and +0.1 V (OCP) *vs* Ag|AgCl, respectively, favoring the emission of solvated electrons. Interestingly, solvated electrons are also measured at 0.8 V *vs* Ag|AgCl, although it corresponds to an upward band bending of +0.4 V.

Upward surface band bending could also be induced by nitrogen doping. The higher doping state level rises the Fermi level in the bulk electrode. Electrons from the doping states, about 1.7 eV below the CBM, can be excited by visible light from about 730 nm. The nitrogen atoms naturally contained in detonation nanodiamonds may then explain their ability to emit solvated electrons in water under visible light illumination.[16,20] Similarly, it has been shown recently that shallow nitrogen-vacancy (NV) centers can also be excited to produce photocurrent response for wavelengths reaching up to 594 nm.[53] Finally, nitrogen-doped ultrananocrystalline diamond have a near-IR response, particularly useful for neuronal interfacing, and also influenced by the surface termination.[30,54,55]

The role of surface termination on the sub-bandgap photo-redox reaction was then investigated. Fluorination is an efficient technique to passivate the diamond surface and suppress most of the inter-band surface states.[48] Hence, F-BDD was used as reference to isolate the sub-bandgap contribution to the photocurrent on H-BDD and O-BDD. Difference photocurrent spectra, subtracted for a similar band bending, are shown in fig. 4a. These spectra were fitted by four Gaussian functions as shown in fig. 4b and c at the energies 4.19 ± 0.1 (blue), 4.83 ± 0.1 (green), 4.8 ± 0.2 (yellow), and 5.38 ± 0.1 eV (red). More details about this procedure can be found in the fig. S5.

For negative band bending, the photocurrent is positive, corresponding to photoreduction reactions of the oxidized surface states, forming C-H terminations:

$$Diam - OH + H_2O + 2e^- \rightarrow Diam - H + 2HO^- \qquad (2)$$

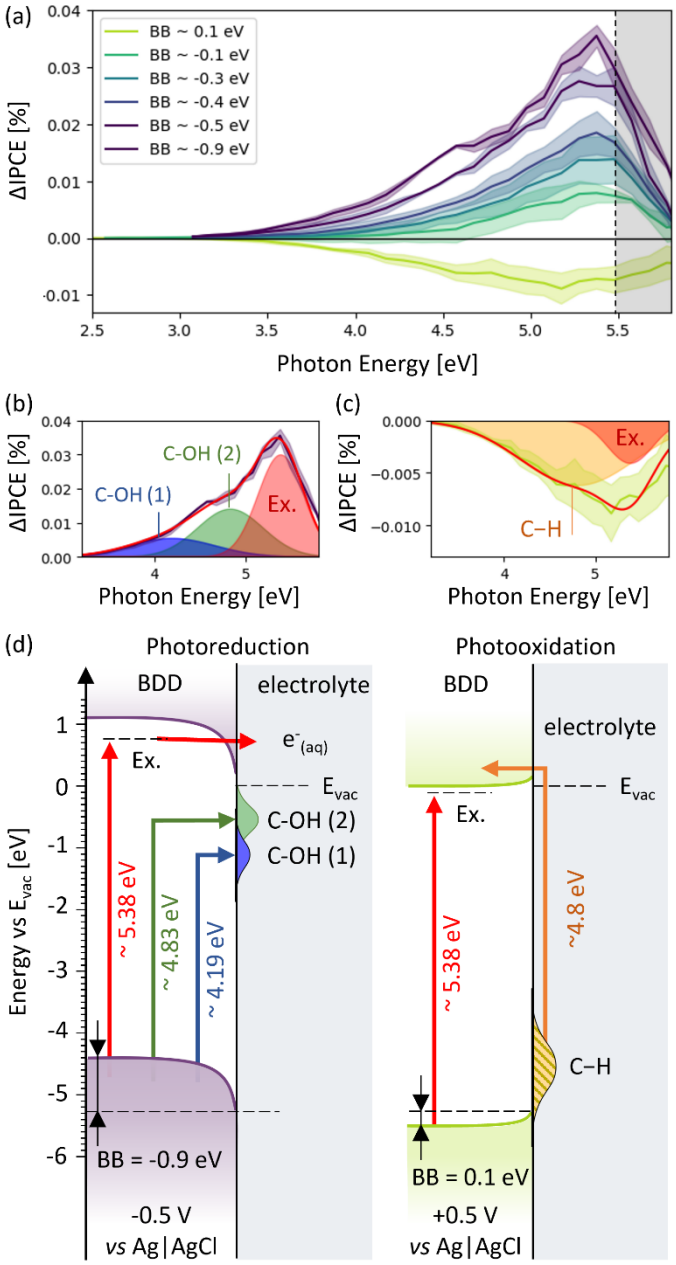

Figure 4: Photoexcitation of diamond electrodes below the bandgap. (a) Difference ($\Delta IPCE$) between the photocurrent measured on O-BDD/H-BDD and the photocurrent measured on F-BDD for a similar band bending. Fit of $\Delta IPCE$ corresponding to the band bendings -0.9 eV (b) and 0.1 eV (c) according to the four identified resonant photoexcitations represented in (d) involving OH surface states and excitonic states (Ex.).

The fit of the photocurrent shows in fact two photoexcitation processes around 4.2 and 4.8 eV (blue and green in fig. 4**b**) labelled C-OH (1) and C-OH (2) in fig. 4**d**. These energies correspond to the excitation of VB electrons to the C-OH unoccupied surface states measured by X-ray absorption spectroscopy (fig. 7) as well as the transitions E_1 and E_2 at 4.2 and 4.9 eV previously reported in air[24]. The difference in energy observed between these two states could be due to the

(de)protonation of the hydroxyl group in water or to a different oxygen bonding configuration such as ether or carboxyl groups, especially on acid treated surfaces.[56]

For positive band bending, the photocurrent is negative, corresponding to photooxidation of the surface according to the opposite reaction. The fit of the photocurrent shows a single photoexcitation around 4.8 eV (yellow in fig. 4c) corresponding to the excitation of electrons from the C-H occupied surface states to the CB as represented in fig. 4d. In air, this transition was also detected between 4.6 and 4.8 eV[24].

The amplitudes of these components strongly depend on the band bending (see fig. S5). A downward band bending favors the photoreduction reactions by pulling the holes away from the surface, thereby limiting charge recombination. While an upward band bending favors the photooxidation reactions by pulling electrons away from the surface.

The fourth process occurring around 5.4 eV (red) corresponds to the excitation of electrons from the VB to an excitonic state of the CB. More precisely, its energy appears close to $E_g - E_x - h\nu_{TA}$ = 5.32 eV, where E_g, E_x, and $h\nu_{TA}$ are the energies of the bandgap (5.47 eV), of the indirect exciton (0.07 eV) and the transversal acoustic phonon (0.083).[24,57–59] This process is stronger on O-BDD compared to F-BDD possibly because the exciton formation and/or dissociation depends on the surface termination, as observed in air.[24] When the exciton dissociates, charge separation is induced by the surface band bending, leading to a photocurrent positive for downward band bending and negative for upward band bending (see fig. S5).

4.3. Redox Reactions probed by Photocurrent

The oxidation and reduction of the surface states of diamond electrodes significantly impact the interface properties by altering the EA and the band bending. Possible redox reactions of the surface states must be considered to determine the stability of the surface under given electrochemical conditions, as well as the electrochemical properties of the electrode, whether under illumination or not.

Photocurrent-cyclic voltammetry (PC-CV) experiments were performed under constant illumination with a light energy of 3.2 eV, using a tunable LED source in 0.5 M KCl. Fig. 5a presents the first three cycles of the CV measured on O-BDD, showing the surface capacitive behavior typical of BDD electrode.[18] The cycles are largely repeatable, indicating good surface stability. No clear redox peaks are observed because no redox couple was introduced into the electrolyte, and the decrease in cell current after the first cycle at negative potentials is likely due to the reduction of oxygen present in the solution. Signs of reduction reactions (Red.), indicated by the blue arrow, are suggested by a broad increase in current around -0.4 V *vs* Ag|AgCl. A small photocurrent (< 20 nA) due to the modulated illumination is also observed (inset fig. 5a) but does not alter the electrochemical behavior of the electrode. The sub-bandgap excitation suggests that the photocurrent originates from the excitation of the surface states. As just demonstrated, the amplitude and sign of this photocurrent are directly correlated with the surface band bending.

Figure fig. 5b represents the photocurrent along the CV extracted from the third cycle. Details about the reconstruction of the PC-CVs from the raw electrochemical CVs are given in the SI fig. S2. The more positive (negative) the applied potential, the more negative (positive) the photocurrent, as the upward (downward) band bending is increased. The FBP can be measured when the photocurrent is zero. The hysteresis observed is due to the electrochemical reduction ("Red.") and spontaneous oxidation ("Ox.") of the surface having a direct impact on its EA and on the FBP. The FBP of the oxidized and reduced surfaces are $FBP_O = +0.52 \pm 0.05V$ and $FBP_H = -0.11 \pm 0.01V$ respectively. These values are close to the ones determined by the *Schottky barrier* model earlier. FBP_O is slightly more positive as the electrochemical oxidation is more pronounced compared to the chemical acid oxidation. FBP_H is not as negative, as a fully reduced surface is unstable and starts to spontaneously oxidize for potentials above -0.6 V *vs* Ag|AgCl. The spontaneous oxidation of the surface is particularly hard to observe on the CV. In a conventional CV, the increase in current due to redox reactions is mixed with other processes such as the variation of the band bending and charge diffusion in the electrolyte. Plotting the photocurrent vs I_{cell} enables to isolate the redox reactions as they only impact I_{cell} but not the photocurrent (fig. 5c). The very broad transition "Red." in the CV appears extremely sharp in this plot. As soon as the potential decreases below -0.4 V *vs* Ag|AgCl, the photocurrent/current ratio completely drops as I_{cell} is strongly increased by the occurring electroreduction of the surface. However, no strong evolution of the photocurrent is observed in fig. 5b confirming the electrochemical nature of the oxidation. Similarly, in the other half of the cycle, the smaller transition Ox. can be observed at -0.6 V vs Ag|AgCl.

Detecting the oxidation of the surface starting at such a low potential may appear surprising at first. To better visualize the reduction (Red.) and oxidation (Ox.) of the surface, fig. 5d and e shows the band alignment at the reduced and oxidized diamond-water interfaces in the condition of "Ox." and "Red.". The EA of the surfaces (-0.86 eV and -0.15 eV, respectively) are deduced from the measured ionization energy E_i presented in the SI tab. S1. The position of the Fermi level in the bulk of the electrode is set by the doping level about 0.39 eV above the VB. The left scale of the applied potential (E_{we}) is corrected for the potential drop in the cell (as detailed in SI section 8) so that the Fermi levels in flat band conditions correspond to the measured value FBP_H and FBP_O (black arrows). The oxidized surface (fig. 5e) starts to reduce when $E_{we}^{Red.}$ = -0.4 V *vs* Ag|AgCl (dashed blue line) because the Fermi level reached the redox potential of H^+/H_2around pH~7. However, the reduced surface (fig. 5d) starts to oxidize when $E_{we}^{Ox.}$ = -0.6 V *vs* Ag|AgCl (dashed red line) while the Fermi level is still above any oxidant couple in the electrolyte. Under these conditions, the Fermi level drops below the level of the occupied CH surface states, leading to charge transfer and favoring the oxidation of the surface.

Without any applied potential, the Fermi level of the diamond surface is in equilibrium with the water and corresponds to the

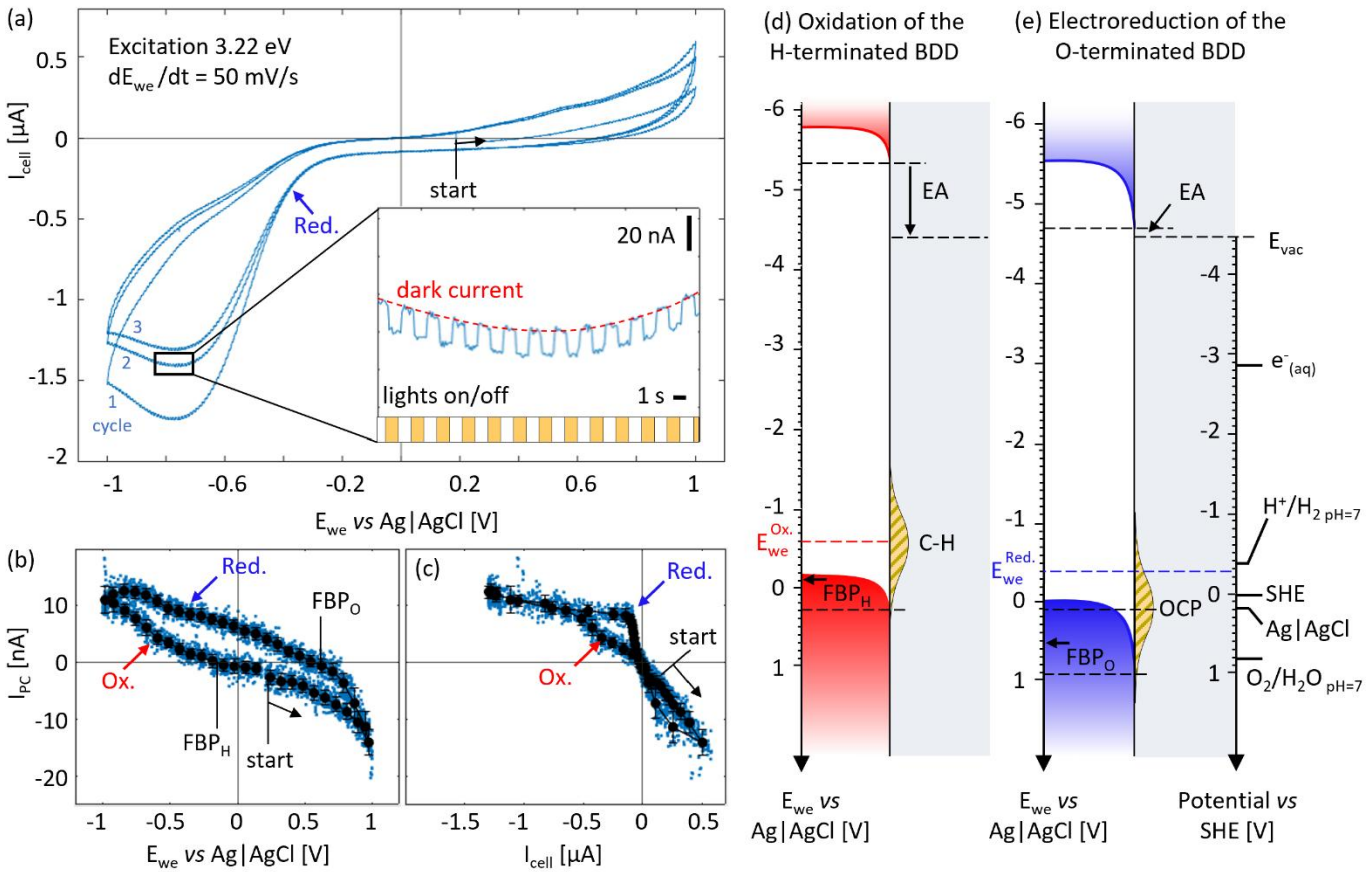

Figure 5: Probing surface redox reactions on diamond with photocurrent. (a) Cyclic voltammetry (CV) on O-BDD between -1 and 1 V *vs* Ag|AgCl (starting positively from the OCP) at a scan rate of 50 mV/s. Numbers indicate the first, second and third cycle. Inset shows a zoom of the photocurrent modulation. Photocurrent-cyclic voltammetry (PC-CV) showing the extracted photocurrent along the third CV cycle (b) and corresponding photocurrent-current plot (c). Black dots represent the local average values. The arrows labeled "Red." and "Ox." indicate the starting points of the electrochemical reduction and spontaneous oxidation of the surface. Band alignment at the diamond-water interface in the case of an electrochemically reduced surface (d) and oxidized surface (e) at the applied potentials of "Ox." and "Red.", respectively. The electron affinity EA of the surface is deduced from the measured ionization energy E_i. The E_{we} scale is aligned with the potential *vs* standard hydrogen electrode (SHE) in the electrolyte using the correction of the potential drop from the SI section 8.

OCP usually measured around +0.1 V vs Ag|AgCl (see section sec. 4.1). Here, the surface spontaneously oxidizes in water until reaching a new equilibrium. While oxidizing, the EA of the surface increases, shifting the position of the remaining occupied CH states until they match the Fermi level. The oxidation of the surface is hence self-limited. In particular, the remaining CH groups of the O-BDD are stable because the EA of this surface is about 0.7 eV lower than the one of the hydrogenated surface, matching the OCP (fig. 5e).

Consequently, electrochemical oxidation appears more efficient than acidic treatment to remove diamond hydrogen termination in aqueous media because lowering the pH shifts the equilibrium potential (-59.2 mV/pH) and further stabilizes the hydrogenated surface.[14] Yet, to obtain a fully hydrogenated surface under our conditions without an applied potential, the pH would need to be far below 0, making these considerations and the Nernst equation irrelevant. Conversely, when a hydrogenated diamond surface is put in water, its oxidation leads to a decrease of the solution's pH.[8,41] PC-CV therefore enabled us to probe fundamental properties of the diamond surface termination directly in liquid and under potential and will be applied to probe functionalized diamond and other photoelectrodes in the future.

https://doi.org/10.26434/chemrxiv-2025-47rf0 **ORCID:** https://orcid.org/0000-0003-2338-1523

Conclusion

In this study, we have demonstrated that charge transfer reactions at the diamond-water interface can be precisely modulated by applying external potential and photoexcitation. Electrochemically-induced surface redox reactions, which lead to the formation of hydroxylated or hydrogenated surfaces, can be employed to control the electron affinity and adjust the band bending at the diamond-electrolyte interface. However, the hydrogenated surface of boron-doped diamond is unstable in water and spontaneously oxidizes until a new equilibrium is reached, depending on the electron affinity and the pH of the solution.

The electrochemical tuning of band bending and surface chemistry allows for fine control of the photoexcitation of the electrode. Resonant photoexcitation of electronic transitions in the UV/Vis range enables controlled photochemical reactions at the diamond-water interface. The emission of solvated electrons has been evidenced for excitation above the bandgap and can be modulated by tuning the surface band bending. We have shown that boron-doped diamond electrodes behave like Schottky barriers, with the potential barrier being tunable by the surface states. The observed large amount of charge recombination provides room for improving the incident photon-to-current efficiency.

A comprehensive understanding of the interfacial photo- and electrochemical processes on boron-doped diamond electrodes in equilibrium with the electrolyte paves the way for new engineered solutions. Rational design of novel diamond-based electrodes may open new avenues for photoelectrochemical generation of solar fuels, water remediation, plastic reforming reactions, or even photo-rechargeable energy storage devices. For instance, functionalizing the diamond surface with appropriate molecules, altering the aqueous microenvironment (pH, redox couples, etc.), or doping the diamond with heteroatoms other than boron may enable photoreactions in the visible range without the necessity of applying any external potential.

5. Author contributions

Arsène Chemin Conceptualization, Data curation (Photocurrent spectroscopy, XAS), Formal Analysis, Investigation, Methodology, Visualization, Writing - original draft, Writing - review & editing

Louis Godeffroy Data curation (Solvated electron dosage), Formal Analysis, Investigation, Visualization, Writing - original draft, Writing - review & editing

Marin Rusu Data curation (Photoelectron yield spectroscopy), Formal Analysis, Writing - review & editing

Michael Drisch Resources (Fluorination of the BDD surface)

Maik Finze Resources (Fluorination of the BDD surface), Writing - review & editing

Peter Knittel Funding acquisition, Resources (production of the nanostructured diamonds), Writing - review & editing

Anke Krueger Resources (Fluorination of the BDD surface), Writing - review & editing

Tristan Petit Funding acquisition, Project administration, Resources, Writing - original draft, Writing - review & editing

6. Conflicts of interest

The authors declare no conflict of interest.

7. Data availability

The data that support the findings of this study are available from the corresponding author upon reasonable request.

8. Acknowledgments

This work was funded by a Freigeist Fellowship from the Volkswagen Foundation (n° 89592) and Horizon2020 project DIACAT (contract 665085) of the European Commission. We thank Patricia Quellmalz, Dr. Christian Giese and Dr. Johannes Ackermann for preparing the diamond surface electrodes. We are grateful to Dr. Steffen Fengler and Dr. Thomas Dittrich for their development of the photocurrent monochromator, and Dr. Ronny Golnak for providing the UV-vis spectrometer used for fluorometry, which made this study possible. X-ray absorption spectroscopy was conducted at the BESSY II synchrotron on the LiXEdrom beamline with the assistance of Dr. Ronny Golnak and Dr. Jie Xiao. We also thank Dr. Thomas Unold for providing access to the PYS measurement setup. The authors thank Solvay Fluor GmbH for generous donations of elemental fluorine and anhydrous HF.

9. Methods and Materials

9.1. Nanostructured Boron-doped Diamond

The electrodes are made from a polycrystalline boron-doped diamond wafer nanostructured by reactive ion etching after dewetting a metal mask. The average doping is 5700 ppm (10^{21} cm^{-3}).[17] The hydrogen termination (referred to as H-BDD) is initially obtained by exposing the sample to hydrogen plasma treatment at a temperature of 700°C. The oxidized termination (referred to as O-BDD) is obtained by wet chemical treatment in a mixture of conc. sulfuric acid and nitric acid (ratio 3:1) for 1.5 h at elevated temperatures, about 250°C.

9.2. Fluorination procedure

Caution! *Elemental F_2 and anhydrous HF (aHF) are highly toxic and can cause severe injuries via skin and eye contact or inhalation. Therefore, all manipulations of these chemicals have to be performed under a well-ventilated fume hood. Wearing of protective gloves, an apron, and a head screen is strongly recommended. All apparatus must be checked carefully for any leaks before starting any reactions.*

Fluorinated termination (referred to as F-BDD), is obtained by fluorination in liquid HF containing 30% of elemental fluorine and subsequent removal of volatile perfluorinated hydrocarbons by evaporation under vacuum. Elemental fluorine

and anhydrous HF (aHF) were obtained from Solvay Fluor GmbH and used as received.

Fluorine and aHF were kept in stainless-steel lines of known volume equipped with capacitance pressure gauges (type 280E Setra Instruments, Acton, MA) and with bellow valves (type BPV25004 Balzers and type SS4BG Nupro Swagelok), as well as with Gyrolok and Cajon fittings. Fluorination reactions in aHF were performed in 100 mL reactors consisting of a PFA bulb with a NS29 socket standard taper (Bohlender, Lauda, Germany) in connection with a PFA NS29 cone standard taper and a PFA needle valve (type 204-30 Galtek, fluoroware, Chaska, MN). The parts were held together with a metal compression flange.

A 100 mL PFA round bottom flask reactor equipped with a magnetic stirring bar was charged with the diamond sample and 10 mL of aHF. The suspension was stirred and cooled to -78°C and vacuum was applied for 5 minutes. Elemental fluorine (3.3 mmol, 40mol%) was added at -78 °C. The suspension was warmed to 50 °C and stirred for five days. After the removal of HF and all other volatiles under reduced pressure, the diamond was dried in a vacuum until all volatile fluorinated side products were removed.

9.3. X-ray absorption spectroscopy (XAS)

X-ray absorption spectroscopy (XAS) was performed at BESSY II synchrotron in Berlin on the U49/2-PGM1 undulator beamline using the ultrahigh vacuum LiXEdrom experimental station, described in detail elsewhere[59]. The measurements were conducted in the electron yield (EY) mode, where the incident photon energy was swept and the drain current, due to the emitted electrons from the sample, were simultaneously recorded by a Keithkey 6514 ammeter. The spectra were normalized by the incident photon flux and between 286 and 290.5 eV. The energy resolution of the monochromator in the range of the C 1s (~ 285 eV) X-ray absorption edges was ~75 meV.

9.4. Photocurrent spectroscopy

The BDD electrodes were utilized as the working electrode (WE) in a spectroelectrochemical flow cell (SEC-3F, C3-Analysentechnik). The electrode area is 0.8 mm². It is contacted by a copper tape via the doped silicon substrate used for the deposition. The low resistivity of the substrate (0.01–0.02 Ω.cm) insures the ohmic contact. The counter electrode (CE) was a stainless-steel tube with a surface area of approximately 75 mm². The potential on the WE was set relative to an Ag|AgCl reference electrode using an SP-200 potentiostat (Biologic), with the current recorded. A positive current indicated the flow of negative charge from the WE to the CE. All photocurrent measurements were performed in an aqueous 3 M KCl electrolyte, transparent up to photon energies of ~5.9 eV. Modulated illumination was provided by a laser-driven light source (LDLS EQ-99X-CAL-S, Hamamatsu) with a custom quartz prism monochromator (T. Dittrich, S. Fengler), covering photon energies between 0.45 and 6.2 eV at a modulation frequency of 1.8 Hz. The FHWM achieved by the monochromator under working conditions is about 0.05 eV. The modulated photocurrent was measured using a lock-in amplifier (EG&G 5210). The photocurrent spectra were normalized to light intensity measured in the same condition using a S130VC Photodiode Power Sensor from Thorlabs corrected from its responsivity. Because each spectrum acquisition takes about 1 h, partial oxidation of the hydrogenated surface is observed. To limit electrochemical modification of the surface upon measurement of the photocurrent spectra, each of the spectra is recorded from the OCP toward the largest polarization where electrochemistry happens, as discussed in the result section.

For the dynamic measurement of the photocurrent on the CV (PC-CV), a large intensity LED at 3.22 eV (pE-4000, CoolLED) was used.

9.5. Fluorimetric titration of solvated electrons

The titration of solvated electrons was achieved by fluorimetry, using a protocol adapted from ref.[50]. The setup was the same as for photocurrent spectroscopy, but instead of using a 3 M KCl electrolyte, the KCl concentration was decreased to 0.1 M to avoid interferences, and 2 mM of KNO_3 (Sigma-Aldrich) was added. The NO_3^- ions serve as scavengers for the solvated electrons to form NO_2^- ions:

$$NO_3^- + 2e_{aq}^- + H_2O \rightarrow NO_2^- + 2HO^- \qquad (3)$$

After one hour of continuous illumination at a given applied potential and light energy, the electrolyte was recovered from the cell. From the ca. 100 μL contained in the cell, 50 μL were taken and mixed with 25 μ L of 0.48 mM 2,3-diaminonaphthalene (2,3-DAN, Sigma-Aldrich) solution (in 0.63 N HCl, Carl Roth). In this step, 2,3-DAN reacts with the NO_2^- ion to form 1-[H]-naphthotriazole.

After 10 min incubation in the dark and at room temperature, 25 μL of 1.32 M NaOH (J.T.Baker) solution were added to the mixture and the latter was further diluted with 1000 μL of 0.44 M NaOH solution. Under these conditions, 1-[H]-naphthotriazole exhibits a strong fluorescence signal at 405 nm when excited at 365 nm as shown in fig. 13a. By comparing the fluorescence intensity measured at 405 nm to a calibration curve (fig. 13b) obtained with known amounts of $NaNO_2$ (in 0.1 M KCl, Sigma-Aldrich), the NO_2^- concentration in the cell could be determined with a 0.1 μM precision.

The fluorimeter used in this study consisted of an UV-vis spectrometer (Ocean SR6, OceanOptics) coupled to a tunable LED light source (pE-4000, CoolLED) facing perpendicularly. Since no filter was used to remove the elastically scattered light from the source, a strong peak can be observed at 365 nm in all fluorescence spectra, even in the absence of 2,3-DAN.

References

1 J. H. Montoya, L. C. Seitz, P. Chakthranont, A. Vojvodic, T. F. Jaramillo and J. K. Nørskov, *Nature Materials*, 2016, **16**, 70–81.

2 Jenny Schneider, Detlef Bahnemann, Jinhua Ye, Gianluca Li Puma, Dionysios D Dionysiou, Jenny Schneider, Detlef Bahnemann, Jinhua Ye, Gianluca Li Puma and Dionysios D

Dionysiou, *Part 1 Fundamental Aspects of Photocatalysis*, 2016.
3 Brian O'Regan and Michael Grätzel, *Nature*, 1991, **353**, 737–740.
4 Q. Guo, C. Zhou, Z. Ma and X. Yang, *Advanced Materials*, 2019, **31**, 50.
5 Guiji Liu, Fan Zheng, Junrui Li, Guosong Zeng, Yifan Ye, David M. Larson, Junko Yano, Ethan J. Crumlin, Joel W. Ager, Linwang Wang, Francesca M. Toma, *Nat Energy*, 2021, **6**, 1124-1132
6 A. G. Tamirat, J. Rick, A. A. Dubale, W. N. Su and B. J. Hwang, *Nanoscale Horizons*, 2016, **1**, 243–267.
7 Y. Piekner, D. S. Ellis, D. A. Grave, A. Tsyganok and A. Rothschild, *Energy & Environmental Science*, 2021, **14**, 4584–4598.
8 W. A. Smith, I. D. Sharp, N. C. Strandwitz and J. Bisquert, *Energy and Environmental Science*, 2015, **8**, 2851–2862.
9 A. M. Ganose, D. O. Scanlon, A. Walsh and R. L. Z. Hoye, Nature, 2022, **13**, 4715.
10 W. Jaegermann, B. Kaiser, J. Ziegler and J. Klett, in *Photoelectrochemical solar fuel production: From basic principles to advanced devices*, Springer International Publishing, 2016, pp. 199–280.
11 J. H. T. Luong, K. B. Male and J. D. Glennon, *Analyst*, 2009, 134, 1965–1979.
12 S. J. Cobb, Z. J. Ayres and J. V. Macpherson, *Annual Review of Analytical Chemistry*, 2018, **11**, 463–484.
13 M. Elisabeth and K. Anke, *Accounts of Chemical Research*, 2022, **55**, 3594–3604.
14 Yasuaki Einaga, *Accounts of Chemical Research*, 2022, **55**, 3605–3615.
15 B. F. Bachman, D. Zhu, J. Bandy, L. Zhang and R. J. Hamers, *ACS Measurement Science Au*, 2022, **2**, 46-56.
16 F. Buchner, T. Kirschbaum, A. Venerosy, H. Girard, J.-C. Arnault, B. Kiendl, A. Krueger, K. Larsson, A. Bande, T. Petit and C. Merschjann, *Nanoscale*, 2022, **14**, 17188.
17 D. Zhu, L. Zhang, R. E. Ruther and R. J. Hamers, *Nature Materials*, 2013, **12**, 836–841.
18 P. Knittel, F. Buchner, E. Hadzifejzovic, C. Giese, P. Quellmalz, R. Seidel, T. Petit, B. Iliev, T. J. S. Schubert, C. E. Nebel and J. S. Foord, *ChemCatChem*, 2020, **12**, 5548–5557.
19 L. Zhang, D. Zhu, G. M. Nathanson and R. J. Hamers, *Angewandte Chemie*, 2014, **126**, 9904–9908.
20 T. Yoshikawa, H. Asakawa, T. Matsumoto, K. Ichikawa, A. Kaga, S. Yamamoto, R. Izumi, M. Ohno, T. Mahiko, M. Mutsuda, S. Yamasaki and N. Tokuda, *Carbon*, 2024, **218**, 118689.
21 N. Roy, Y. Hirano, H. Kuriyama, P. Sudhagar, N. Suzuki, K. I. Katsumata, K. Nakata, T. Kondo, M. Yuasa, I. Serizawa, T. Takayama, A. Kudo, A. Fujishima and C. Terashima, *Scientific Reports*, 2016, **6**, 38010.
22 Z. Shpilman, I. Gouzman, T. K. Minton, L. Shen, A. Stacey, J. Orwa, S. Prawer, B. C. C. Cowie and A. Hoffman, *Diamond and Related Materials*, 2014, **45**, 20–27.
23 M. Sobaszek, M. Brzhezinskaya, A. Olejnik, V. Mortet, M. Alam, M. Sawczak, M. Ficek, M. Gazda, Z. Weiss and R. Bogdanowicz, *Small*, 2023, **19**, 26, 2208265.
24 A. Chemin, I. Levine, M. Rusu, R. Vaujour, P. Knittel, P. Reinke, K. Hinrichs, T. Unold, T. Dittrich and T. Petit, *Small Methods*, 2023, **7**, 11, 2300423.
25 K. Patel, K. Hashimoto and A. Fujishima, *Journal of Photochemistry and Photobiology A: Chemistry*, 1992, **65,** 419-429.
26 A. Y. Sakharava, Y. V. Pleskav, F. Di Quarto, S. Piazza, C. Sunseri, I. G. Teremetskaya and V. P. Varnin, 1995, *J. Electrochem*. Soc. **142,** 2704.
27 L. Boonma, T. Yano, D. A. Tryk, K. Hashimoto and A. Fujishima, 1997, *J. Electrochem. Soc.* **144,** L142.
28 Y. V. Pleskov, V. M. Mazin, Y. E. Evstefeeva, V. P. Varnin, I. G. Teremetskaya and V. A. Laptev, 2000, *Electrochem. Solid-State Lett*., **3,** 141.
29 A. Chambers, S. Prawer, A. Ahnood and H. Zhan, *Frontiers in Chemistry*, 2022, **10**.
30 A. Chambers, A. Ahnood, S. Falahatdoost, S. Yianni, D. Hoxley, B. C. Johnson, D. J. Garrett, S. Tomljenovic-Hanic and S. Prawer, *Diamond and Related Materials*, 2020, **103**.
31 A. Ahnood, A. N. Simonov, J. S. Laird, M. I. Maturana, K. Ganesan, A. Stacey, M. R. Ibbotson, L. Spiccia and S. Prawer, *Applied Physics Letters*, 2016, **108**, 104103.
32 S. Falahatdoost, A. Chambers, A. Stacey, H. N. Al Hashem, A. Nadarajah, S. Prawer and A. Ahnood, *Applied Surface Science*, 2021, **543**, 148768.
33 J. Raymakers, K. Haenen and W. Maes, *J. Mater. Chem. C*, 2019,**7**, 10134-10165.
34 Z. Jian, N. Yang, M. Vogel, Z. Zhou, G. Zhao, P. Kienitz, A. Schulte, H. Schönherr, T. Jiao, W. Zhang and X. Jiang, *Small Methods*, 2020, **4**, 9, 2000257.
35 M. Mastellone, A. Bellucci, M. Girolami, V. Serpente, R. Polini, S. Orlando, A. Santagata, E. Sani, F. Hitzel and D. M. Trucchi, *Nano Letters*, 2021, **21**, 4477–4483.
36 A. F. Sartori, S. Orlando, A. Bellucci, D. M. Trucchi, S. Abrahami, T. Boehme, T. Hantschel, W. Vandervorst and J. G. Buijnsters, *ACS Applied Materials and Interfaces*, 2018, **10**, 43236–43251.
37 M. Girolami, A. Bellucci, M. Mastellone, S. Orlando, V. Serpente, V. Valentini, R. Polini, E. Sani, T. De Caro and D. M. Trucchi, *Materials*, 2020, **13**, 1–12.
38 F. Maier, J. Ristein and L. Ley, *Phys. Rev. B*, **64**, 165411.
39 D. Miliaieva, A. S. Djoumessi, J. Čermák, K. Kolářová, M. Schaal, F. Otto, E. Shagieva, O. Romanyuk, J. Pangrác, J. Kuliček, V. Nádaždy, Š. Stehlík, A. Kromka, H. Hoppe and B. Rezek, *Nanoscale Advances*, 2023, **5**, 4402–4414.
40 V. V. S. S. Srikanth, P. S. Kumar and V. B. Kumar, *International Journal of Electrochemistry*, 2012, **1**, 2090-3537.
41 V. Chakrapani, J. C. Angus, A. B. Anderson, S. D. Wolter, B. R. Stoner and G. U. Sumanasekera, *Science*, 2007, **318**, 1424–1430.
42 M. Dankerl, A. Lippert, S. Birner, E. U. Stützel, M. Stutzmann and J. A. Garrido, *Physical Review Letters*, 2021, **106,** 196103.
43 J. A. Garrido, A. Härtl, M. Dankerl, A. Reitinger, M. Eickhoff, A. Helwig, G. Müller and M. Stutzmann, *Journal of the American Chemical Society*, 2008, **130**, 4177–4181.
44 A. Härtl, J. A. Garrido, S. Nowy, R. Zimmermann, C. Werner, D. Horinek, R. Netz and M. Stutzmann, *Journal of the American Chemical Society*, 2007, **129**, 1287–1292.
45 S.R. Morrison, *Electrochemistry at Semiconductor and Oxidized Metal Electrodes*, 1980, Springer.
46 A. Chemin, M. K. Kuntumalla, M. Brzhezinskaya, T. Petit and A. Hoffman, *Applied Surface Science*, 2024, **661**, 160082.
47 R. Malkinson, M. K. Kuntumalla, A. Hoffman and N. Bar-Gill, *Journal of Materials Chemistry C*, 2023, **12**, 7206–7213.
48 E. M. Zagrebina, A. V. Generalov, A. Y. Klyushin, K. A. Simonov, N. A. Vinogradov, M. Dubois, L. Frezet, N. Mårtensson, A. B. Preobrajenski and A. S. Vinogradov, *Journal of Physical Chemistry C*, 2015, **119**, 835–844.
49 J. F. Morar, F. J. Himpsel, G. Hollinger, J. L. Jordon, G. Hughes and F. R. McFeely, *Physical Review B*, 1986, **33**, 1346–1349.
50 J. B. Cui, J. Ristein and L. Ley, 1999, *Phys. Rev. B,* **60**, 16135.
51 F. Ducrozet, E. Brun, H. A. Girard, J. C. Arnault and C. Sicard-Roselli, *Journal of Physical Chemistry C*, 2023, **127**, 19544–19553.
52 A. Hankin, F. E. Bedoya-Lora, J. C. Alexander, A. Regoutz and G. H. Kelsall, *J. Mater. Chem. A*, 2019, **7**, 26162-26176

53 K. Xu, D. Pagliero, G. I. López-Morales, J. Flick, A. Wolcott and C. A. Meriles, *ACS Applied Materials & Interfaces*, 2024, **16**, 37226–37233.
54 S. Falahatdoost, A. Chambers, A. Stacey, S. Prawer and A. Ahnood, *Surfaces and Interfaces*, 2022, **30**, 101850.
55 A. Chambers, S. Prawer and A. Ahnood, *Journal of The Electrochemical Society*, 2023, **170**, 026502.
56 S. Ferro, M. Dal Colle and A. De Battisti, *Carbon*, 2005, **43**, 1191–1203.
57 C. D. Clark, P. J. Dean and P. V. Harris, *Proc. R. Soc. Lond. A*, 1964, **277**, 312–329.
58 Dittrich Thomas, *AIP Advances*, 2022, **12**, 065206.
59 T. Dittrich and S. Fengler*, Semicond. Sci. Technol.*, 2023, **38** 015015